Article

Yttrium-Doped Iron Oxide Nanoparticles for Magnetic Hyperthermia Applications

Przemyslaw Kowalik, Jakub Mikulski, Anna Borodziuk, Magdalena Duda, Izabela Kamińska, Karolina Zajdel, Jaroslaw Rybusinski, Jacek Szczytko, Tomasz Wojciechowski, Kamil Sobczak, Roman Minikayev, Magdalena Kulpa-Greszta, Robert Pazik, Paulina Grzaczkowska, Krzysztof Fronc, Mariusz Lapinski, Małgorzata Frontczak-Baniewicz, and Bozena Sikora*

Cite This: *J. Phys. Chem. C* 2020, 124, 6871−6883

Read Online

ACCESS | Metrics & More | Article Recommendations | SI Supporting Information

ABSTRACT: Magnetic nanoparticles of Fe_3O_4 doped by different amounts of Y^{3+} (0, 0.1, 1, and 10%) ions were designed to obtain maximum heating efficiency in magnetic hyperthermia for cancer treatment. Single-phase formation was evident by X-ray diffraction measurements. An improved magnetization value was obtained for the Fe_3O_4 sample with 1% Y^{3+} doping. The specific absorption rate (SAR) and intrinsic loss of power (ILP) values for prepared colloids were obtained in water. The best results were estimated for Fe_3O_4 with 0.1% Y^{3+} ions (SAR = 194 W/g and ILP = 1.85 nHm^2/kg for a magnetic field of 16 kA/m with the frequency of 413 kHz). The excellent biocompatibility with low cell cytotoxicity of Fe_3O_4:Y nanoparticles was observed. Immediately after magnetic hyperthermia treatment with Fe_3O_4:0.1%Y, a decrease in 4T1 cells' viability was observed (77% for 35 μg/mL and 68% for 100 μg/mL). These results suggest that nanoparticles of Fe_3O_4 doped by Y^{3+} ions are suitable for biomedical applications, especially for hyperthermia treatment.
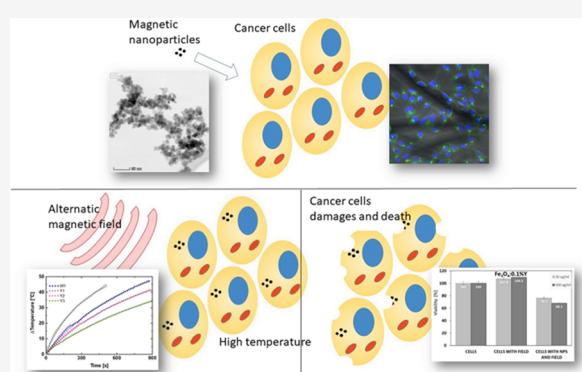
1. INTRODUCTION

Magnetic iron oxide nanoparticles (NPs) already attracted a significant scientific interest due to their exceptional magnetic properties showing great potential in bio-related applications. The most commonly studied are hematite (α-Fe_2O_3: rhombohedral crystal structure), maghemite (γ-Fe_2O_3: cubic), and magnetite (Fe_3O_4), which is isostructural with γ-Fe_2O_3 with one important feature relying on iron cations having two different valence states (Fe^{2+} and Fe^{3+} with a ratio of 1:2). Among all of them, the most interesting are maghemite and magnetite due to their ferrimagnetic character, which by far surpasses the magnetic behavior of hematite. Fe_3O_4 belongs to the spinel ferrite family with a general chemical formula of AB_2O_4 and crystallizes in a cubic system ($Fd\bar{3}m$ space group). The main disadvantage in contrast to maghemite can be found as a potential risk of complete Fe^{2+} oxidation into Fe^{3+} resulting in a chemical transformation of Fe_3O_4 ($FeFe_2O_4$) into γ-Fe_2O_3 or even α-Fe_2O_3.[1] Unfortunately, the oxidation step between Fe_3O_4 and γ-Fe_2O_3 can be hardly detected by the X-ray powder diffraction technique since their diffraction patterns are pretty much the same and the sample color does not differ that much as well (dark brown or even black). It is much easier to recognize whether Fe_3O_4 transformed into α-Fe_2O_3 since the latter one crystallizes in a rhombohedral system ($R\bar{3}c$) giving a totally different diffraction and there is a significant change in a sample

color (from dark almost black brown into red). The importance of this critical issue has several straightforward consequences: (1) change in magnetic behavior, which is critical in view of potential bio-related applications; (2) an oxidation process itself, which leads to the well-known Fenton reaction, creation of the reactive oxide species (ROS), and programmed cell death; and (3) lack of chemical stability of the material itself, which can be detrimental to the engineered material properties (efficacy of the heat induction).

Previous studies have shown that ferrite NPs have already attracted considerable attention due to their outstanding magnetic properties and high prospect in biomedical applications such as magnetic drug delivery, magnetic resonance imaging, magnetic separation, or hyperthermia.[2−6] Despite the issues described above, magnetite NPs are used in cancer diagnostics and therapy[3,7] and were also approved by the Food and Drug Administration (FDA) as contrast agents in magnetic

resonance. In addition, the second and third phases of clinical research using Fe_3O_4 NPs in hyperthermia as cancer therapy are already carried out in Germany with a lack of noticeable toxic effects.[8]

Fe_3O_4 has an inverse spinel structure. Large oxygen ions are tightly packed in a cubic order, while smaller Fe^{3+} ions fill completely the eight sites of the tetrahedral subnetwork. The octahedral positions are occupied by Fe^{2+} and Fe^{3+} ions. Because the magnetic spins of the tetra- and octahedral networks are arranged in the opposite direction, the structure is ferrimagnetic.[9] Magnetic properties of magnetite result from the separation of 5d orbitals. Orbitals are divided into subgroups due to the presence of a field of ligands, in this case, oxide. This means that all Fe^{3+} and Fe^{2+} ions have one pair of paired electrons and four unpaired electrons. In octahedral coordination (where the d orbit divides into two subgroups E_g and T_{2g}), iron ions are ferromagnetically coupled via a so-called double exchange mechanism. One of the electrons from a paired pair can be exchanged between two octahedral coordinates. In contrast, Fe^{3+} ions in tetra- and octahedral sites are coupled antiferromagnetically by an oxygen atom, which means that Fe^{3+} spins zero each other, so only unpaired Fe^{2+} spins in an octahedral coordination contribute to magnetization.[10]

The Fe^{2+} ions in Fe_3O_4 can be replaced with another divalent transition metal M^{2+} (for example, M = Zn, Mn, Ni, Co, Cu, etc.), which gives MFe_2O_4 ferrite an inverted spinel structure. The magnetization is dependent mainly on unpaired d electrons from M^{2+}. However, when M^{2+} is small enough, MFe_2O_4 can adopt a spinel structure in which two Fe^{3+} occupy octahedral sites, and M^{2+} occupies tetrahedral sites, and there is no antiferromagnetic coupling between the two Fe^{3+} ions. The structure provides a higher magnetization value than that of the reverse spinel structure of MFe_2O_4.[11−16]

Iron ion nanoparticles doped with metal ions, such as $CoFe_2O_4$, $NiFe_2O_4$, and $MnFe_2O_4$, have strong magnetic properties and improved, for example, contrast effects in magnetic resonance imaging (MRI), which are much better than those of conventional Fe_3O_4 NPs.[17] Nevertheless, the use of these M^{2+}-doped iron oxide nanoparticles in biomedical research is severely hampered by the high levels of toxicity associated with the presence of these transition metals (Co, Ni, and Mn).[18−20]

One of the widely studied dopants is Zn ions to iron oxide nanoparticles, which have a high magnetization value, which significantly increases their MRI contrast and hyperthermic effects. Their initial *in vitro* and *in vivo* studies showed that Zn^{2+}-doped Fe_3O_4 is non-toxic and potentially useful in biology and medicine.[21,22]

Another type of Fe_3O_4 dopant used to improve magnetic properties is lanthanide ions (Ln^{3+}). Lanthanide ions are an interesting class of dopants due to the unique optical and magnetic properties associated with their f electron configurations.[23,24] Magnetite doping can change its magnetic, dielectric, and structural properties by adding, e.g., trivalent cations such as Nd^{3+}, Cr^{3+}, Y^{3+}, or In^{3+}. Rare-earth cations such as La^{3+}, Sm^{3+}, or Dy^{3+}, by substituting Fe^{3+} in the octahedral position, release iron ions to coordinate in the tetrahedral position, which alleviates the lattice tension. Due to this, the amount and type of Ln^{3+} doping changed the magnetization, permeability, and electrical resistance of magnetite.[25−32] For example, Milanović et al.[25] observed decreasing saturation magnetization after In^{3+} ion doping of $ZnFe_2O_4$, but after Y^{3+} ion doping, they observed increasing magnetization compared with

undoped NPs but only for small amount of dopants (0.15%). They suggest that Y^{3+} ions stabilize Fe^{3+} ions in the octahedral sites, thus reducing the tendency toward inversion.[25]

In the work, Fe_3O_4 NP doping with yttrium ions was used to increase the magnetization of the material for magnetic hyperthermia treatment. The addition of yttrium ions reaches their maximum in the range from 1 to 1.5 mol % (relative to moles of Fe^{3+}). With a further increase of the dopant, the second nanocrystalline phase precipitates. For now, the Fe_3O_4 NP doping by Y^{3+} ions was not investigated for a magnetic increase and hyperthermia application.

Hyperthermia is a therapeutic procedure based on heating the selected tissue above normal physiological temperatures. It can be sought as an alternative cancer therapy that induces less side effects in contrast to radio- or chemotherapy. Hyperthermia is usually carried out in two distinct temperature regimes:[33−36] (1) at high temperature, above 48 °C for an irreversible treatment of cancer cells. The effect of temperature is drastic and non-reversible, highly efficient but risky due to collateral damages with possible tumor or tissue total ablation upon exceeding the vaporization temperature of water.[36,37] (2) A clinically relevant temperature ranging at 41−48 °C for hyperthermia treatment leads to protein denaturation, cell function inactivation, oxidative stress, or rapid necrotic cell death.[38] During therapy, cell apoptosis or thermal shock protein expression is induced; tissue processes include changes in pH or perfusion and oxygenation of the tumor microenvironment. The effectiveness of the therapy mainly depends on the achieved temperature, time of exposure, and characteristics of the cancer cells.[39]

For the most advantageous feature of hyperthermia in neoplastic disease treatment compared with classic techniques like surgery, chemotherapy, and radiotherapy, hyperthermia tends to be less invasive but has to be combined with traditional methods in order to increase overall efficacy. However, treatment toward recovery from cancer requires localized, controlled, and efficient heating. This important task can be fulfilled by designing and developing alternative techniques utilizing nanoparticle-based systems for non-contact heating by specific stimulation for heat induction.

In the case of magnetic nanoparticles for magnetothermal therapy, heating is realized by taking advantage of their magnetic properties. Generally speaking, the effect can be achieved by using an alternating magnetic field (AMF) on NPs, which will eventually heat up inductively due to the following mechanisms originating from power loss under the AMF:

(1) Hysteresis losses during the irreversible magnetization process (usually can be estimated by taking into account the area of the hysteresis loop), which work mostly for particles that are not in the superparamagnetic state (no area of loop, no contribution of this mechanism in total particle heating, a characteristic for particles with a size above the superparamagnetic regime)

(2) Eddy currents, but this depends strongly on the electric conductivity of the material; once the dielectric material is taken into account, this type of loss has very low contribution (ferrites' case).[40]

(3) So-called residual losses being identified specifically as Néel and Brownian relaxations, which are strongly dependent on particle size, shape, agglomeration, etc.[41]

When the particles are in a superparamagnetic state, i.e., they are below the certain critical particle size (for Fe_3O_4, approximately 30 nm),[42] residual losses (Néel and Brownian

relaxations) upon magnetization—demagnetization cycles[5] are dominant in heat generation. The Néel relaxation mechanism refers to the rotating of the magnetic moments within each particle (inner particle relaxation), whereas Brownian relaxation is connected with rotation of the entire nanoparticle with the setting of magnetic moments in accordance with the field direction (outer particle relaxation).[43,44]

The magnetic nanoparticles (MNPs) are introduced into the cells by endocytosis. The leaky vasculature of cancerous tissue absorbs larger amounts of MNPs than those of normal tissue.[45,46] Moreover, the biomolecules such as antibodies can be easily attached to the MNPs. In addition, MNPs like iron oxides can be used as a magnetic factor in multifunctional nanoconstructs for use in diagnostic imaging capabilities and targeting drugs.[47,48]

The main aim of present studies was to synthesize stable Fe_3O_4 NPs doped with Y^{3+} ions by using a fast and efficient single-step process, which will be suitable for magnetic hyperthermia treatment with one ultimate goal relying on investigations of cell viability after magnetic hyperthermia treatment on breast cancer 4T1 cells.

2. EXPERIMENTAL METHODS

2.1. Synthesis. All chemicals were purchased from Sigma-Aldrich. For the synthesis of Fe_3O_4 NPs, 8 mmol of $FeCl_3·6H_2O$ and 4 mmol of $FeSO_4·7H_2O$ were dissolved in water and sonicated for 30 min. Then, 5 mL of NH_4OH (25%) was added at a rate of approximately 2 drops/min. The mixture was sonicated for 10 min and then centrifuged and washed twice with ethanol/water (1/4). The product was finally washed with water to get rid of the ammonia residue.

The syntheses of Y^{3+}-doped Fe_3O_4 NPs were carried out analogously to the synthesis of the Fe_3O_4 sample. The Y^{3+} ions were added to the starting materials with appropriate molar ratios of Y^{3+} calculated from the formula: $Y^{3+}_xFe^{2+}Fe^{3+}_{2-x}O_4$. For 0.1% Y^{3+}, 0.004 mmol of $YCl_3·6H_2O$ was added, for 1% Y^{3+}, 0.04 mmol of $YCl_3·6H_2O$, for 10% Y^{3+}, 0.4 mmol of $YCl_3·6H_2O$, and for 50% Y^{3+}, 2 mmol of $YCl_3·6H_2O$ were added.

2.2. X-ray Diffractometry (XRD), Transmission Electron Microscopy (TEM), and Scanning Electron Microscopy (SEM) Characterization. X-ray powder diffraction measurements of the Fe_3O_4:Y samples were performed by using a Philips X'Pert Pro Alpha1 MPD (Panalytical) laboratory diffractometer using Cu Kα1 radiation, in the wide 2θ range. The samples' crystallographic properties were analyzed by Rietveld refinement with help of the Fullprof 2k program (Rodriguez-Carvajal, J., 2016, FullProf, ver. 5.8).

The particle size and morphology of samples were also determined by SEM using a Zeiss Auriga Neon 40 microscope at an acceleration voltage of 5 kV.

HR TEM investigations were conducted on an FEI Talos F200X transmission microscope at 200 kV. The measurements were performed in TEM and STEM modes using high-angle annular dark field imaging (HAADF). An energy-dispersive X-ray spectroscopy (EDX) detector was used for mapping element distribution. The samples for the TEM observations were prepared by dropping the colloid particle dispersion on a carbon film supported on a 300 mesh copper grid.

2.3. Magnetic Characterization. Magnetization measurements including saturation magnetization, zero-field cooling (ZFC), and field cooling (FC) measurements were performed on a Quantum Design MPMS XL - 7 SQUID magnetometer. FC-ZFC measurements were collected in the range of 2.0 to 300.0 K at an applied magnetic field of 20.0 mT. Field dependent hysteresis loops of magnetization (M—H) were measured at a temperature of 310.0 K with an applied field range from 0 to 5.0 T.

2.4. Hyperthermia Measurements. The specific absorption rate (SAR) and intrinsic loss of power (ILP) of the pure magnetic colloids (concentration of 3 mg/mL in 1.5 mL) were measured with a commercial AC field generator (DM100 by nB nanoscale Biomagnetics, Spain) working at f = 413 kHz and field amplitude H_0 of 16 kA/m.

2.5. Cell Culture. All *in vitro* studies were carried out with 4T1 cells (mice mammary gland cancer cells; ATCC CRL2539). Initially, 4T1 cells were grown in Dulbecco's Modified Eagle Medium (DMEM) supplemented with 10% v/v of fetal bovine serum at 37 °C in a humidified atmosphere of 5% CO_2.

2.6. *In Vitro* Toxicity Study. To determine the cell viability, different colorimetric assays (i.e., MTT, Presto Blue, CyQuant, Live/Dead) were used. The 4T1 cells were cultured through the night in 96-well plates (10,000 cells/well) at 37 °C and 5% CO_2. Subsequently, cells were incubated with fresh medium containing different concentrations of MNPs (0, 5, 10, 25, and 35 mg/mL) for 16 h. Cells treated only with medium served as negative controls. After incubation with MNPs, media of each well were removed, and cells were washed twice with PBS (only from wells designed for CyQuant assay, we removed only 50% of medium and left over 100 μL of medium). Then, cells were treated:

For MTT assays, 150 μL of MTT in DMEM solution (10% of MTT stock solution reagent, 5 mg/1 mL) to each well was added. After 3 h of incubation, the medium was removed, and created formazan crystals were dissolved in dimethyl sulfoxide (100 μL of DMSO/well).

For PrestoBlue assay, 100 μL of 10% PrestoBlue reagent in DMEM solution was added and left in the incubator for 1 h.

For CyQuant assay, to each well (containing 100 μL of non-removed DMEM), 97.6 μL of fresh DMEM with 0.4 μL of direct nucleic acid stain and 2 μL of direct background suppressor was added and incubated for 1 h.

For live/dead assay, cells were incubated for 45 min with 99.75 μL of PBS solution with 0.05 μL of calcein and 0.2 μL of ethidium homodimer-1.

The plate was read using a Promega GLOMAX Discover GM3000 microplate reader, for MTT assay, with an absorbance mode at a wavelength of 560 nm; the others assays were read in the fluorescence mode with different excitation wavelength and emission wavelength ranges depending on assays used, i.e., ex = 520 nm, em = 580−640 nm (PrestoBlue); ex = 475 nm, em = 500−550 nm (CyQuant); ex = 475 nm, em = 500−550 nm; and ex = 520 nm, em = 580−640 nm. All experiments were performed four times. Results are given as means (with standard deviations) of the values obtained in these four repetitions.

2.7. *In Vitro* Hyperthermia Measurements. For *in vitro* magnetic hyperthermia experiments, 4T1 cells were cultured as described above and seeded into cell culture dishes (3.5 mm of diameter) at 10^5 cells/dish with 2 mL of DMEM and incubated overnight. Then, MNP solution was added at concentrations of 35 μg/mL (0.7 ng, 0.003 nmol of MNPs/cell, that is, 0.002 nmol of Fe/cell) or 100 μg/mL (2.0 ng, 0.008 nmol of MNPs/cell, that is, 0.006 nmol of Fe/cell). The additional dishes, each containing cells without MNPs, were used as a control. Cells were incubated for 16 h. Next day, media with and without MNPs were collected from each dish, and cells were washed

three times with PBS to remove the non-incorporated NPs. Cells were flooded by fresh medium and exposed to AMF.

The magnetic hyperthermia experiments on 4T1 cells were divided with the four samples: the first two groups consisting of as-cultured blank 4T1 cells (without MNPs) and MNP-loaded 4T1 cells were not exposed to magnetic fields and were analyzed at the end of the experiment in order to compare the natural viability of the cell culture. The second two groups, blank and MNP-loaded 4T1 cells, were exposed to the AMF at the selected frequency of f = 423 kHz and amplitude H = 16 kA/m, and an application time of 30 min was chosen. All experiments were carried out utilizing the D5 series G2 driver equipped with a PC70 coil and CAT sample holder designed for cell culture measurements (atmosphere and temperature control; nB nanoScale Biomagnetics, Spain). After field exposure, cell viability was measured using MTT assay.

2.8. TEM Imaging of the Fe$_3$O$_4$ MNPs inside the 4T1 Cells. The presence of the Fe$_3$O$_4$ NPs inside the 4T1 cells was confirmed by TEM imaging. Upon incubation with 5 μg/mL Fe$_3$O$_4$ NPs for 16 h, the 4T1 cells pellets were fixed with 2% paraformaldehyde and 2.5% glutaraldehyde in 0.1 M cacodylate buffer, pH = 7.4 at 4 °C for 2 h. The samples were washed three times in cacodylate buffer, post-fixed with 1% osmium tetroxide for 1 h, dehydrated in the graded series of ethanol (from 30% to 99.8%) and propylene oxide, embedded in Epon resin, and polymerized at 60 °C for 24 h. After resin polymerization, the samples were sectioned (60 nm) using a MTXL ultramicrotome (RMC, U.S.A.). The ultrathin sections were collected on copper grids and examined by a JEM-1011 transmission electron microscope (JOEL, Japan). The operating voltage of the microscope was 80 kV.

2.9. Multiphoton Confocal Microscopy Imaging. Immunofluorescence confocal microscopy using a Zeiss 710 NLO system was the main technique for imaging Fe$_3$O$_4$ NPs inside 4T1 cells. The three channels were observed: the first, with excitation at 488 nm (continuous laser) and a detecting range of 495−572 nm, was used to image the lysosomes marked with antibodies conjugated with AlexaFluor488 dye; the second, with excitation at 705 nm (femtosecond laser), was used for imaging the nucleus marked by the Hoechst marker while detecting in the 425−475 nm range; and the third channel for MNPs imaging was performed in a visible light transmission mode. Samples for confocal microscopy imaging were prepared according to the earlier described procedure.[49]

3. RESULTS AND DISCUSSION

3.1. Synthesis and Structural Characterization. The crystal structure was examined by the XRD technique. The diffraction patterns for W1, Y1, Y2, and Y3 samples (Figure 1) are single-phase materials with a spinel structure (space group: $Fd\bar{3}m$). The lattice parameters of the samples were determined using the Rietveld method in the Supporting Information (Table S1) (obtained results can indicate a non-stoichiometric character of the samples).[50] The graphical fitting results can be found in Figure S1 in the Supporting Information. The lattice parameters values are slightly increasing with increasing Y^{3+} concentration. The averaged dimensions of the nanocrystallites were assessed using the Scherrer method:

$$D = \frac{k\lambda}{\cos\Theta\sqrt{\beta^2 - \beta_0^2}}$$

(1)
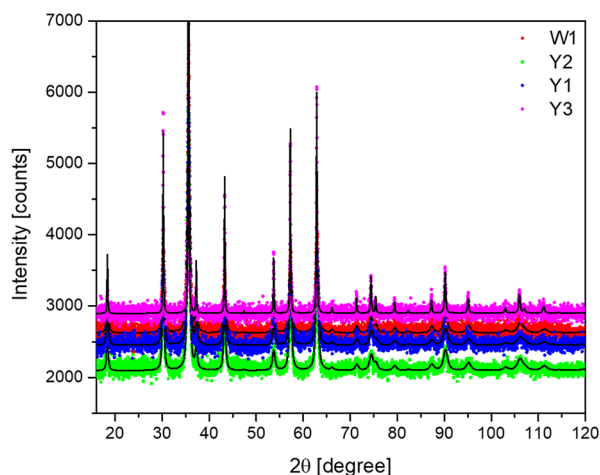
Figure 1. X-ray diffraction patterns of the Fe$_3$O$_4$ NPs as a function of Y^{3+} cation content.

**Table 1. Lattice Parameter a and Nanoparticle Size Extracted from the XRD Data**

sample	percent of Y^{3+}	lattice parameter [Å]	crystallite size [nm]
W1	0%	8.3466(8)	14 ± 3
Y1	0.1%	8.3469(8)	13 ± 2
Y2	1%	8.3467(6)	14 ± 3
Y3	10%	8.3543(2)	56 ± 7

where D is the grain size, β_0 is the apparatus broadening, β is the full width at half maximum, θ is the angle, k is a constant (usually equal to 0.9), and λ is an X-ray wavelength.[51] The results of the Rietveld refinement together with crystallite sizes are gathered in Table 1.

It is well known that the incorporation of the trivalent cations such as Nd^{3+}, Cr^{3+}, Y^{3+}, or In^{3+} into the structure of the magnetite affects strongly magnetic, dielectric, and structural properties of the Fe$_3$O$_4$ NPs. Rare-earth cations such as La^{3+}, Sm^{3+}, or Dy^{3+}, by substituting Fe^{3+} in octahedral position, can force the Fe^{3+} ion for preferential occupation of the tetrahedral crystallographic site. This will ease the crystal lattice tension, and therefore the density of the Fe^{3+} ions will increase the permeability, and as a logical consequence, the resistance of NPs will increase.[25−27] In this work, the intention of using as a dopant Y^{3+} cations was to increase the magnetization of the magnetite. The comparison of the literature data suggests that Y^{3+} will preferentially enter the octahedral sites[29] and, as a result of radius incompatibility (ionic radii: Y^{3+} at eightfold coordination, 1.019 Å and Fe^{3+} at eightfold coordination, 0.78 Å),[52] the cell volume will expand, and therefore the a cell parameter has to increase accordingly.[27] Actually, this trend is consistent with the Rietveld refinement until maximum Y^{3+} concentration is achieved (10 mol %) at the Fe^{3+} octahedral site. This phenomenon (together with charge incompatibility) has to be always taken into account at the stage of the given material synthesis planning.

The sample morphology and particle size of the Fe$_3$O$_4$ NPs doped by the Y^{3+} ions were characterized by using SEM techniques (Figure 2). The normal distribution was fitted to the size distribution histograms obtained from the analysis of SEM images. The size and particle distribution (standard deviation (SD)) were calculated and are presented in Table 2.

As one can see, the W1, Y1, and Y2 materials are composed of polydisperse NPs with SDs of approximately 3−4 nm. It can be
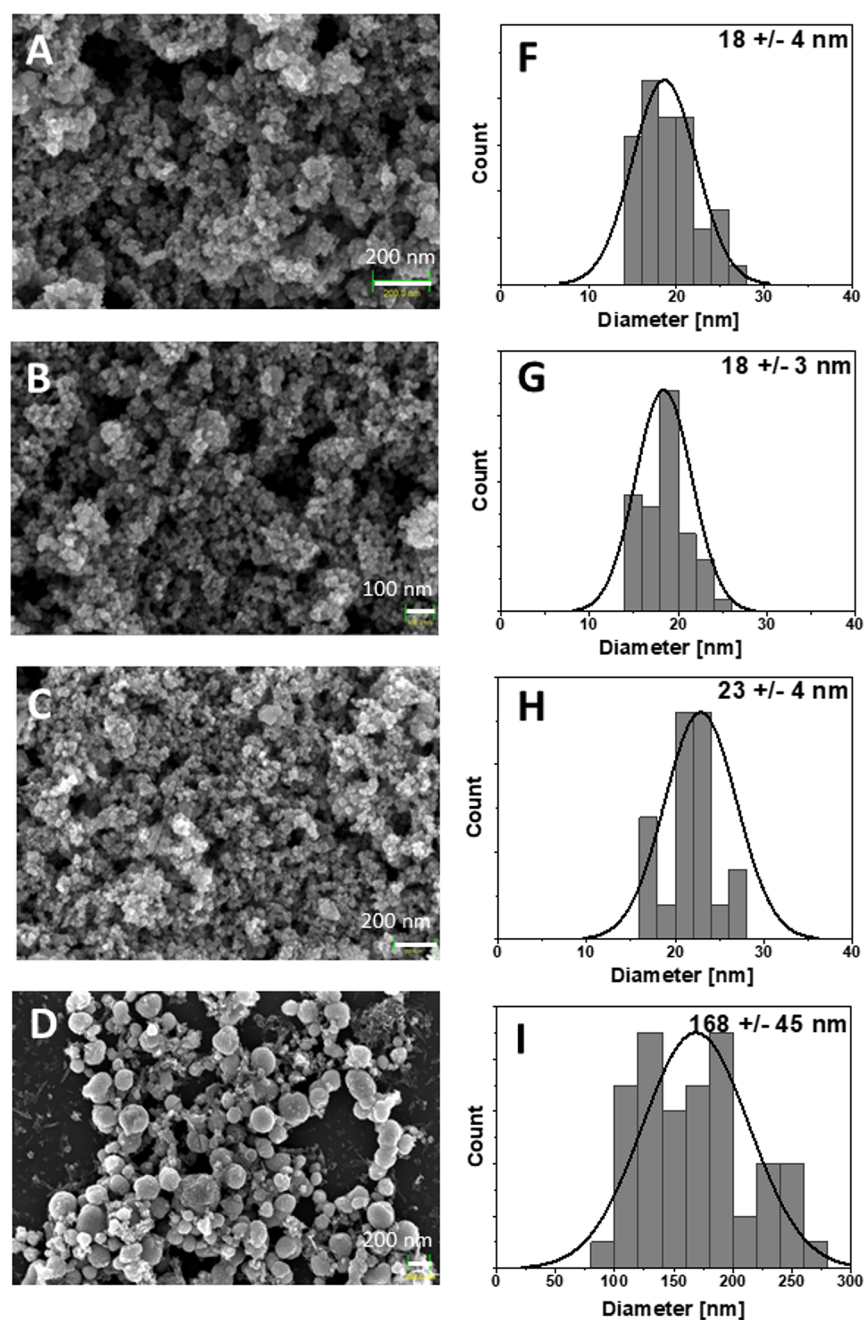
Figure 2. SEM images and histograms of Fe_3O_4 NPs doped by Y^{3+} ions. (A, F) Fe_3O_4 (W1), (B, G) 0.1% Y^{3+}-doped Fe_3O_4 (Y1), (C, H) 1% Y^{3+}-doped Fe_3O_4 (Y2), and (D, I) 10% Y^{3+}-doped Fe_3O_4 (Y3) MNPs.

Table 2. Diameter and Standard Deviation (SD) of the MNPs

sample	diameter [nm]	SD
W1	18	4
Y1	18	3
Y2	23	4
Y3	168	45

noticed that the particle size of the Y1–Y3 magnetite samples doped with yttrium ions increases upon the increase of the Y^{3+} cation content. The mean particle size of the Y3 sample is approximately 170 nm with an SD of 45 nm. This behavior might point out two things: either fast particle growth, which might be promoted by the increased Y^{3+} amount, or the formation of one or several thermodynamically more favored

and stable unknown amorphic phases, which can be more convincingly related. The SEM results clearly indicate particle agglomeration, which is accordance with the TEM results (Figure 3).

Elemental analysis and mapping of the Fe_3O_4 NP compositions was conducted by means of EDX spectroscopy connected with TEM microscopy in order to confirm the crucial ratio between elements (Table 3). As it can be seen, the ratios between iron and oxygen ions are in a good correspondence with theoretical values. The same has been observed in the case of Y^{3+} doping. The results of element mapping are shown in Figure 3. Elemental colocalizations of Fe, Y, and O elements were found indicating the homogenous distribution of all elements within Fe_3O_4 NPs.
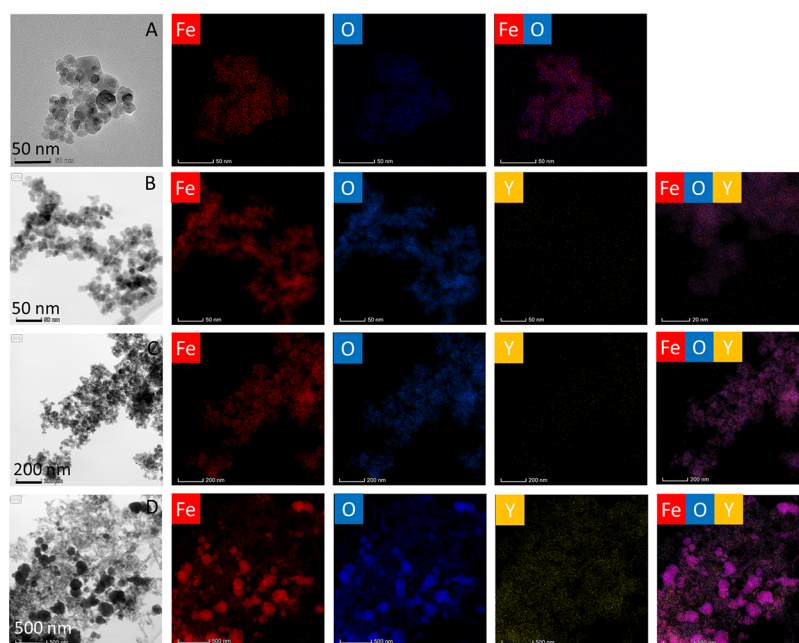
Figure 3. TEM and EDX mapping of Fe_3O_4 NPs doped by Y^{3+} ions. (A) Fe_3O_4 (W1), (B) 0.1% Y^{3+}-doped Fe_3O_4 (Y1), (C) 1% Y^{3+}-doped Fe_3O_4 (Y2), and (D) 10% Y^{3+}-doped Fe_3O_4 (Y3) MNPs.

Table 3. Elemental Analysis of EDX of Fe_3O_4 NPs Doped with Yttrium Ions

| sample | $2Fe^{3+}Fe^{2+}/O^{2-}$ (%) | | $Y^{3+}/2Fe^{3+}Fe^{2+}$ (%) | |
	theoretical value	experimental value	theoretical value	experimental value
W1	75.0	55.2 ± 9.4		
Y1	75.0	53.0 ± 9.1	0.10	0.20 ± 0.02
Y2	74.5	53.4 ± 9.0	0.70	0.70 ± 0.06
Y3	70.3	52.0 ± 9.0	6.80	7.30 ± 0.70

3.2. Magnetic Properties. In order to determine the blocking temperature for the samples, the zero ZFC/FC measurements were performed. After exceeding this temperature, the system becomes superparamagnetic. The ZFC/FC measurements consist of cooling the sample without a magnetic field then slowly heating it in the magnetic field and cooling it again in the same field. The relation between magnetization and temperature was measured (Figure 4A) in the temperature range from 2.0 to 300.0 K in an external magnetic field of 20.0 mT. The blocking temperature was not determined because the samples in the entire temperature range exhibited ferromagnetic properties. This is illustrated by the gap (hysteresis) between the two ZFC/FC graph curves (Figure 4A).

The ferromagnetic properties of the samples were confirmed by the measurement of magnetization (M) as a function of the external magnetic field (B) (Figure 4B,C). The highest magnetization was obtained for the Y2 sample doped with 1 mol % yttrium (75 emu/g). Both samples Y1 and Y2 achieved higher magnetization than that of the sample without Y^{3+} ions, W1. The saturation magnetization of the samples decreased with the higher concentration of Y^{3+} ions (Y3).

Standard error propagation was estimated for SQUID measurements. The accuracy of mass measurement was $\Delta_m = 10^{-4}$ g, and the accuracy of magnetic moment measurement was $\Delta_\mu = 10^{-8}$ emu. The standard deviation of six measurements of $M(B)$ (made at the same temperature) was $\sigma_M = 1$ emu/g. An error account was made using eq 2. The estimated maximal
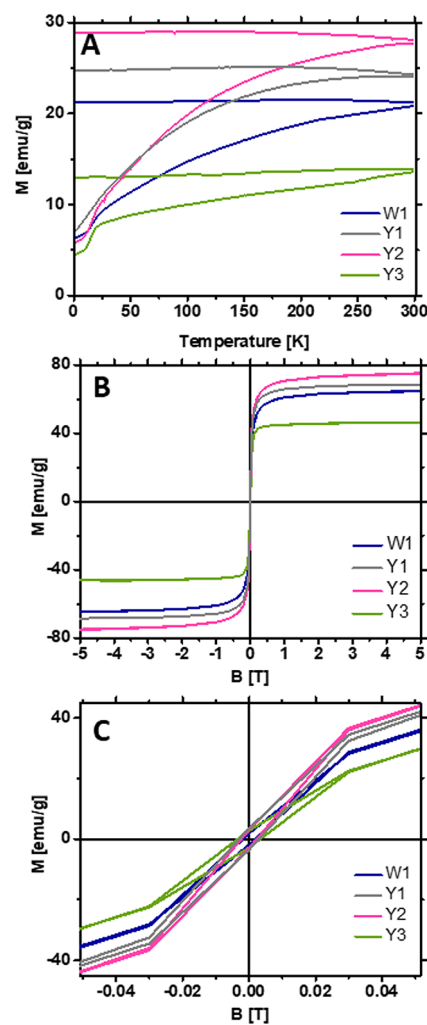
Figure 4. (A) ZFC/FC plot of W1 and Y1−Y3 samples. (B) Hysteresis loops at 310 K. (C) Zoom of the hysteresis loops at 310 K.
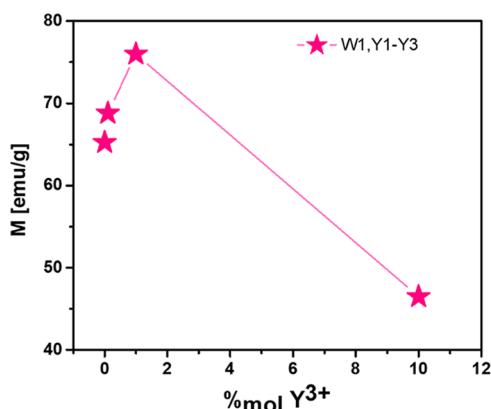
Figure 5. Graph of dependence of magnetization on % yttrium doping. Points are connected by a line to show the trend.
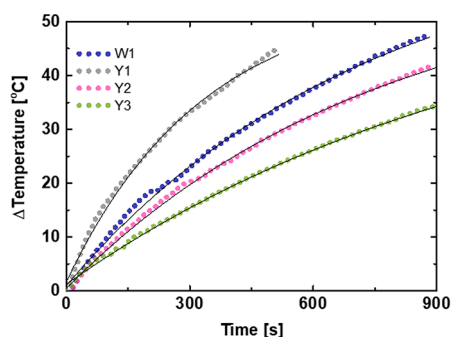

Figure 6. Measurement of the hyperthermic effect for samples W1 and Y1−Y3.

Table 4. SAR and ILP Parameters for Samples W1 and Y1−Y3

sample	SAR (W/g)	ILP (nHm^2/kg)
W1	120 ± 17	1.15 ± 0.09
Y1	194 ± 27	1.85 ± 0.26
Y2	101 ± 14	0.97 ± 0.14
Y3	76 ± 11	0.73 ± 0.10

Table 5. Comparison of ILP Parameters for Y1 and Reference Samples

parameter	Y1	ref[57]	ref[58]	ref[59]	ref[60]
ILP [nHm^2/kg]	1.85 ± 0.26	1.01	0.4	1.21	2.84

measurement uncertainty d_M of the magnetization depending on the magnetic field was 2.5 emu/g.

$$d_M = \sqrt{\frac{1}{3}\left(\frac{\Delta_\mu}{m}\right)^2 + (\sigma_M)^2 + \frac{<\mu>^2 \ \Delta_m^2}{3\,m^4}} \qquad (2)$$

where m is the sample mass and $<\mu>$ is the magnetic moment.

The dependence of samples' saturation magnetization on the concentration of yttrium ions is shown in Figure 5. The maximum magnetization is achieved by the sample Y1 (1% of Y^{3+}), which confirms that the magnetization increases with the doping concentrations to reach the maximum. Then, the magnetization decreases with a further increase of the percentage of doping.

The magnetization of ferrites comes from the difference in the net magnetic moment of the ions at the tetrahedral and octahedral lattice sites. A−B super-exchange interactions prevail over intrasublattice A−A and B−B interactions (Néel model).[53] Therefore, the saturation of magnetization comes from the sum of vectors of the net magnetic moments of the individual A and B sublattices.[26,29,30] The magnetization directly shows the distribution of the Fe^{3+} ions between the two sublattices. If the Fe^{3+} ions occupy both octahedral and tetrahedral sites, the ferrimagnetic ordering will be observed. It is known that the magnetization is higher in MNPs than in bulk materials because of the formation of a partially inversed spinel. The location of Fe^{3+} ions on tetrahedral sites causes Fe^{3+}_A−O−Fe^{3+}_B super-exchange interactions and the increase of magnetization is observed.

By substituting Fe^{3+} ions by non-magnetic Y^{3+} ions, the magnetization of the octahedral coordination should be reduced, resulting in a decrease in magnetization. However, with a small amount of Y^{3+} addition (up to 1%), the trend is opposite. In the case of small Y^{3+} concentrations, the magnetization increases. There are two possible explanations of the observed effect: first, if non-magnetic Y^{3+} ions at low concentrations enter spinel tetrahedral sites, leaving Fe^{3+} in octahedral sites, this can also lead to an increase of magnetization. However, the literature data suggests that Y^{3+} should prefer the octahedral sites.[27,52] Second, the presence of Y^{3+} ions increases the size of nanoparticles, which increases blocking temperature and saturation magnetization for low dopant concentrations. Although further increasing Y^{3+} doping keeps increasing the size of the MNPs, finally, this leads to the decrease of saturation magnetization because non-magnetic yttrium replaces magnetic iron in octahedral sites.[27,52]

3.3. Hyperthermia Effect of MNPs in Solution. The most commonly used parameter for estimation of the heat conversion efficacy on MNPs under action of AMF is the SAR. The SAR is defined as the power (P, measured in W) produced per sample unit mass (m_{MN}, measured in g) (eq 3).

$$SAR = \frac{P}{m_{MN}} \qquad (3)$$

However, the SAR depends on the frequency of the magnetic field (f, measured in Hz) as well as the intensity of the magnetic field (H, measured in kA/m). In order to make possible the comparison of obtained values between different laboratories, it is by far more appropriate to use the so-called ILP (eq 4) parameter. The ILP is given by the simple formula presented below and allows for the presentation of the experimental values regardless of measurement conditions:[54]

$$ILP = \frac{SAR}{fH^2} \qquad (4)$$

Both SAR and ILP parameters contain important information regarding the amount of dispersed heat energy induced by AMF. The exact measurement relies on calorimetric experiments performed under adiabatic conditions. This approach allows for complete minimization of heat exchange, which might occur between the measured system and surroundings. However, this critical condition is very difficult to achieve in a laboratory apparatus (time-consuming). Therefore, in reality, the SAR and ILP are measured under pseudo-adiabatic conditions, and afterward, analytical models are used allowing the most accurate determination of the SAR and/or ILP. In this work, the Box−Lucas (eq 5) model was used, which fits the least squares curve:

$$\Delta T = A(1 - \exp(-\lambda(t + t_0))) \qquad (5)$$
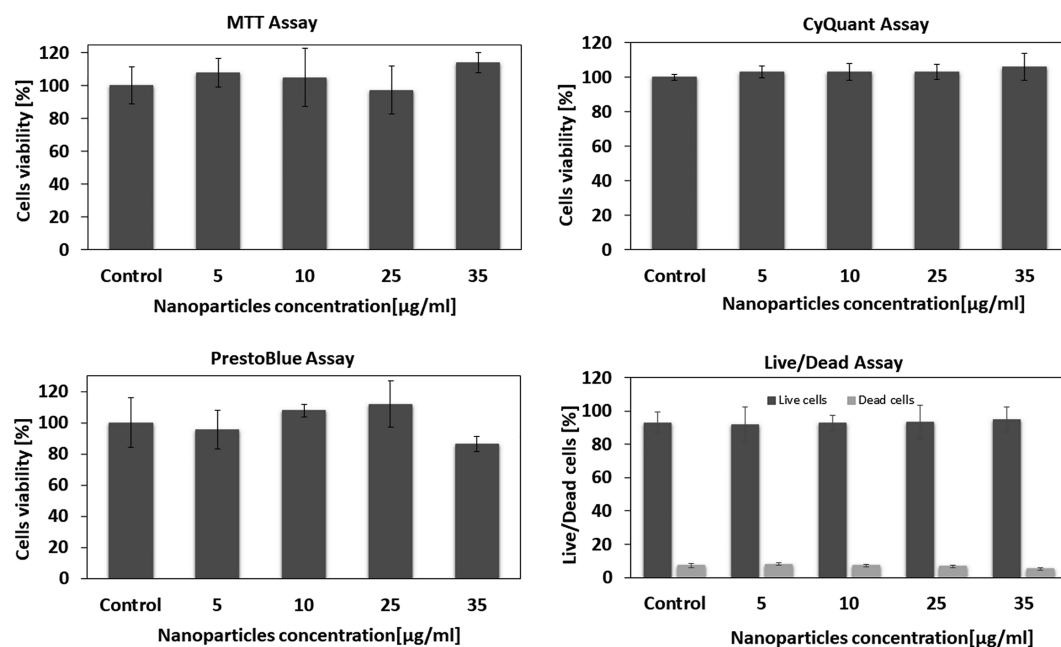
Figure 7. Cell viability values estimated from the MTT, CyQuant, PrestoBlue, and live/dead assays vs the concentration of the Fe$_3$O$_4$ NPs. Cells were incubated with 0−35 μg/mL MNPs at 37 °C for 16 h. Each data point is represented as mean (SD from four trials).

If A and λ are known (from fitting eq 5), then the SAR (eq 6) can be directly calculated where $A\lambda = T_s\tau^{-1} = \frac{P}{C}$, T_s is the temperature, τ^{-1} is the characteristic cooling time, C is the heat capacity of nanoparticles. The starting temperature (t_0) can be omitted in the calculation because it is only taken into account in measurements where the initial temperature difference is different from zero (for the curve graph $\Delta T(t)$).

$$SAR_{Box-Lucas} = \frac{A\lambda C}{m_{MN}} \qquad (6)$$

The applied analytical method causes an error of a few percent, while other analytical methods, such as the distribution method, introduce an error of several percent. Ultimately, these parameters are determined to estimate the quality of the produced MNPs in terms of generated heat, comparing them with the results obtained for another type of nanomaterial.[55]

Measurement of the hyperthermia effect was carried out in an aqueous solution. The samples had a similar concentration of approximately 3 mg/mL. The increase of temperature was measured by a system of optical thermometers with a measuring range of error of ±0.2 °C in an external magnetic field of 16 kA/m with a frequency of 413 kHz. The theoretical model was adapted to the measurement data. Figure 6 shows the increase of temperature as a function of time. The fastest temperature rise was generated by the Y1 sample, which heated the aqueous solution at 45 °C in a very short time (less than 9 min). A similar temperature was obtained by the W1 sample. However, this temperature was achieved after a significantly longer time (almost two times). Application of the theoretical model to recorded data allowed calculation of the SAR and ILP. All values presented in Table 4 correspond to the heat generation rates of the samples. The highest value of the SAR and ILP parameters was obtained from the sample Y1 (SAR = 194 ± 27 W/kg; ILP = 1.85 ± 0.26 nHm^2/kg).

In hyperthermia, the exposure time is an important factor. Therefore, the shorter time of heat generation by MNPs and action of AMF means that they are more suitable for use in magnetic hyperthermia. It can be concluded that the Y1 sample meets these criteria best in comparison with other samples. The ILP value for the Y1 sample is within the range of literature values (Table 5). The ILP of the Y1 sample, compared to the reference iron oxide samples, is generally higher, except for one sample,[56] suggesting its high efficiency in magnetic hyperthermia. It should be noted that the parameters of hyperthermia depend on many factors, including the coverage of nanoparticles and their size, composition, and method of synthesis. Therefore, it is difficult to directly compare the results with the results for the same type of nanoparticles but with different physical properties.

3.4. Cytotoxicity Assays. In order to investigate the cytotoxicity of Fe$_3$O$_4$ NPs on 4T1 cells, several tests (MTT, CyQuant, PrestoBlue, and live/dead assays) were performed (Figure 7). No significant difference in the cell proliferation was observed in the absence or presence of 5−35 μg/mL MNPs in all viability tests (see Figure 7). The cellular viabilities were estimated at approximately 100% in all tests for all concentrations of MNPs. These data show that the Fe$_3$O$_4$ NPs have relatively low cytotoxicity after 16 h of incubation for all concentrations.

3.5. Cellular Uptake Studies. Cellular uptake of MNPs by 4T1 cells was visualized by confocal imaging (Figure 8). Cells stained by the MNPs were visualized at transmitted light. In addition, the 4T1 cells were stained by antibodies to lysosomes conjugated with AlexaFluor 488, green color. The nucleus was stained by Hoechst 33342, blue color. The overlay of the MNP channel and cell channel indicates that the MNPs entered into the cells and locate within the cytoplasm.

The various stages of internalization of the Fe$_3$O$_4$ NPs and their location inside the cells were obtained by TEM measurements (Figure 9). In order to improve MNP uptake, the cellular internalization mechanisms and accumulation of MNPs in murine mammary carcinoma (4T1) cells were studied. The results of the investigation have shown that MNPs have the ability to enter cells via a form of active transport. The Fe$_3$O$_4$ NPs are internalized into the cell by invaginations of the cell
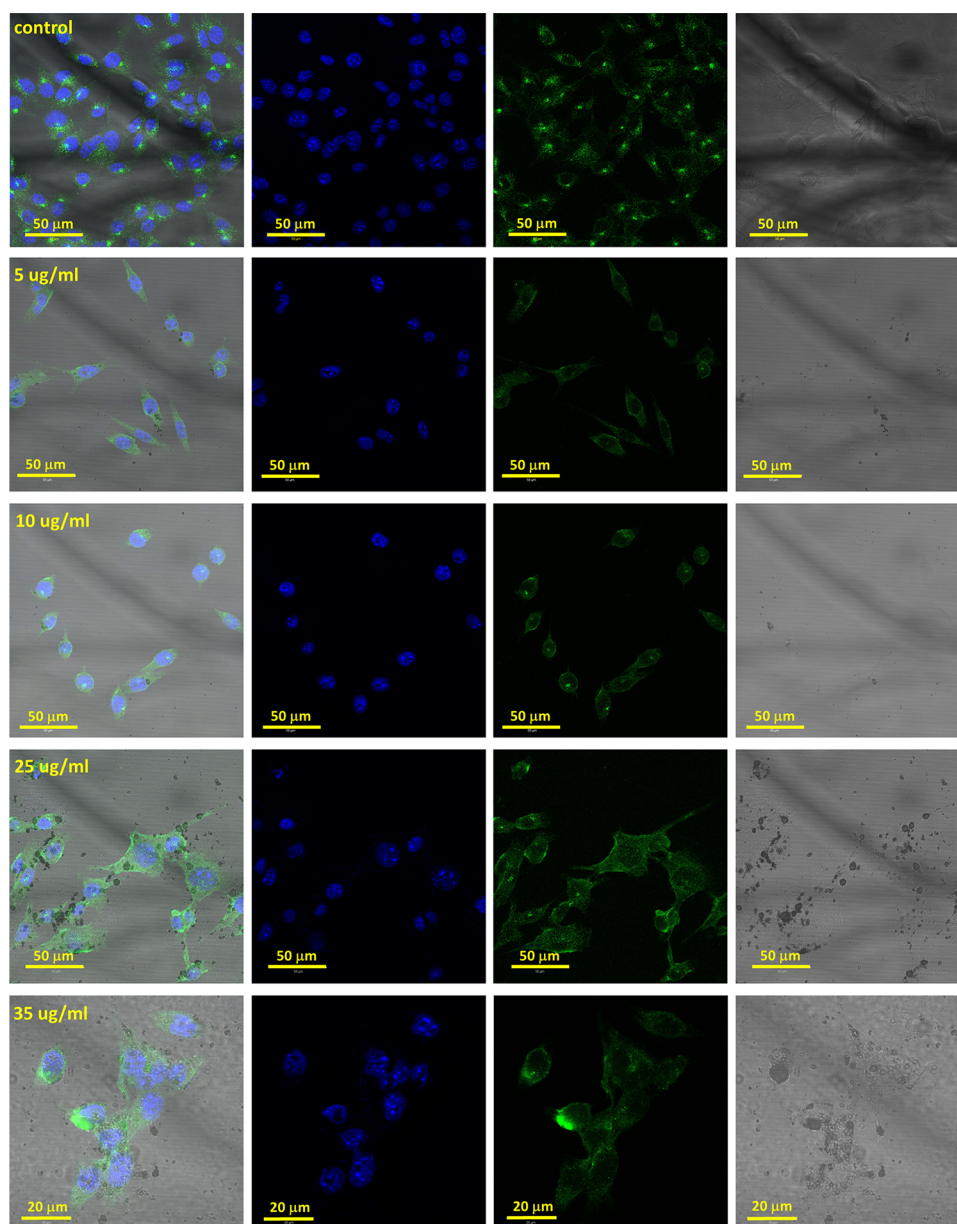
Figure 8. 4T1 cells with Fe_3O_4 NPs depend on the NP concentration. The time of incubation was 16 h. The MNP concentrations were 5, 10, 25, and 35 μg/mL. The blue color indicates the nuclei of the cells. The green color indicates the lysosomes. The Fe_3O_4 NPs were measured in transparent light.

membrane (Figure 9A,B) that surround and enclose MNPs by forming endocytic vesicles. The up-taken MNPs entrapped into intracellular vesicles are next translocated to the perinuclear region of cell. The Fe_3O_4 NPs are never released to the cell cytoplasm but are always localized in selected vesicular organelles such as endosomes or subsequent lysosomes (Figure 9C–H). The above observations suggest that the endocytosis process is involved in cellular internalization of the MNPs. Long-term incubation with MNPs present inside cells did not indicate significant ultrastructural changes in comparison to control cells.

3.6. *In Vitro* Hyperthermia. We studied the effects of Fe_3O_4 and Fe_3O_4:0.1% Y on 4T1 cells in the presence of an AMF based on procedures described previously.[61] 4T1 cells with MNPs (35 and 100 μg/mL) were exposed to a magnetic field for 30 min. The exposure to the magnetic field cells in the absence of MNPs did not show any significant effect on the cell viability. The AMF without MNPs did not cause any damages to the cells. The cell viability was reduced to approximately 85% when the cells were

incubated with 35 μg/mL Fe_3O_4 NPs and to approximately 72% with 100 μg/mL Fe_3O_4 NPs in the presence of the AMF (Figure 10A). However, the viability of the cells was significantly more reduced when the cells were incubated with Fe_3O_4 nanoparticles doped by 0.1% Y^{3+} ions exposed to the AMF (Figure 10B). The Fe_3O_4:0.1% Y NPs with a concentration of 35 μg/mL reduced the cell viability by 77% and with a concentration of 100 μg/mL, reduced the cell viability by 68% when the cells were exposed to the AMF for 30 min (Figure 10B). This implies that the hyperthermia treatment was effective for the Y^{3+}-doping sample more than without doping Fe_3O_4 nanoparticles. Our research showed that Y^{3+}-doped Fe_3O_4 NPs can work much better than without the doping.

Others researchers studied the magnetic hyperthermia effect of MNPs with different sizes and different coatings on cancer cells. For example, Thorat et al.[62] measured the cytotoxicity of polymer-coated $La_{0.7}Sr_{0.3}MnO_3$ MNPs on L929 cancer cells in much higher concentrations until 2 mg/mL. They did not
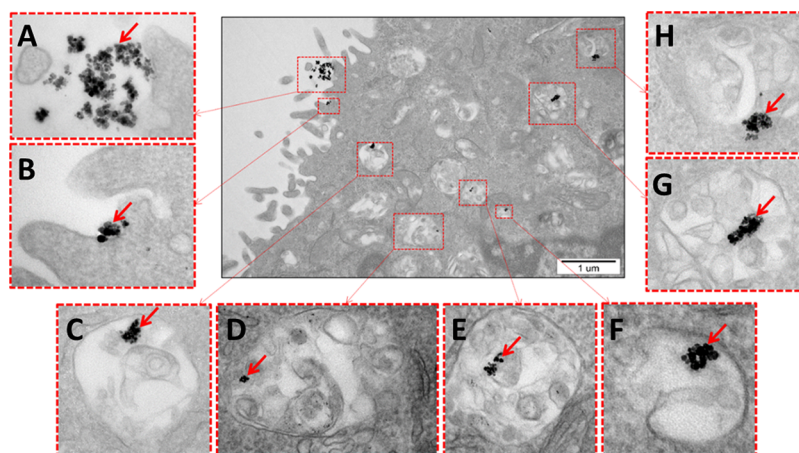
Figure 9. TEM images of the Fe_3O_4 NPs (5 μg/mL) inside the 4T1 cells. (A, B) Various stages of MNP internalization and (C−H) their localization in vesicles after 16 h of incubation at 37 °C (red arrows indicate the nanoparticle aggregates).
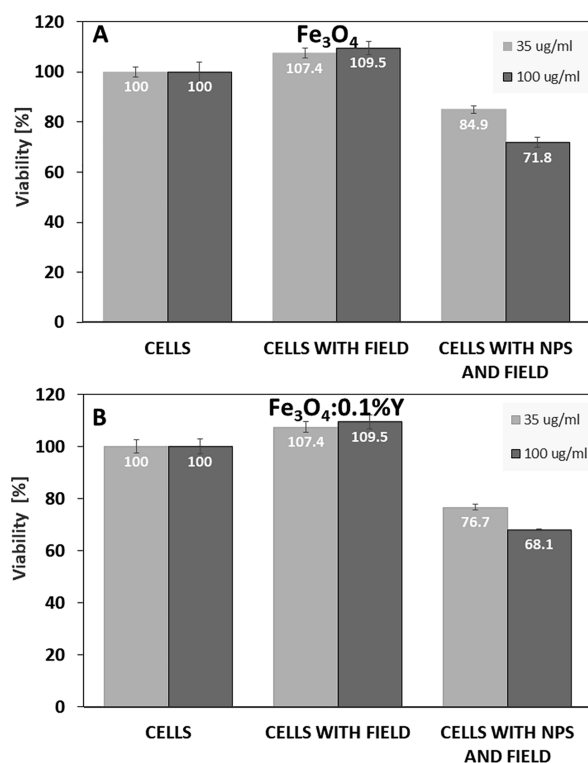
Figure 10. Hyperthermia treatment experiment on the 4T1 cells with (A) Fe_3O_4 and (B) Fe_3O_4:0.1%Y NPs in 35 μg/mL and 100 μg/mL concentrations. The MTT assay was performed directly after applying the magnetic field for 30 min. The applied magnetic field was 20 mT with the frequency of 423 kHz. The temperature of the environment was 37 °C.

observe any toxicity. Patil et al.[63] studied Fe_3O_4 NPs coated with oleic acid and betaine HCl. They observed that more than 60% MCF cells were killed within 20 min of magnetic hyperthermia exposure. The 90 min of hyperthermia exposure was required to kill approximately 86−97% of MCF cells, but the concentration of MNPs they used was much higher than in our case (from 0.1 to 2 mg/mL for 10^5 cells in the cited paper; 35 and 100 μg/mL in this paper). To compare these results, we have to use the same concentration and conditions for the *in vitro* hyperthermia measurements.

4. CONCLUSIONS

The Fe_3O_4 MNPs doped by different amounts of Y^{3+} ions (0, 0.1, 1, and 10%) were synthetized. The crystal structures examined by the XRD technique confirm single-phase spinel ferities for all samples. The MNPs' size increases with the increase of the Y^{3+} cation content. The as-prepared MNPs are ferromagnetic at room temperature. This is illustrated by the gap (hysteresis) between the two ZFC/FC graph curves. The maximum magnetization is achieved by the sample with 1% Y^{3+}, which confirms that the magnetization increases with the doping concentrations to reach the maximum. Then, the magnetization decreases with the further increase of the percentage of doping. The saturation magnetization of the MNPs increases with the increase of Y dopants until reaching 1% Y^{3+}, indicating that the small amount of Y^{3+} ions doped stabilizes Fe^{3+} in octahedral sites, reducing the tendency toward inversion. Then, the decrease of saturation magnetization is observed indicating the lowering of the number of Fe^{3+}_A−O−Fe^{3+}_B superexchange interactions.

The magnetic hyperthermia of MNPs in water was measured. The specific absorption rate (SAR) and intrinsic loss of power (ILP) values were obtained. The best results were estimated for Fe_3O_4 with 0.1% Y^{3+} ions (SAR = 194 W/g and ILP = 1.85 nHm^2/kg). The excellent biocompatibility with low cell cytotoxicity of Fe_3O_4:Y nanoparticles was observed by four independent cytotoxicity tests (MTT, CyQuant, PrestoBlue, and live/dead assays). The cellular viabilities were estimated at 100% in all tests for all concentrations of MNPs. The various stages of internalization of the MNPs and their location inside the cells were obtained by TEM and confocal microscopy measurements. The results of the investigation have shown that MNPs have the ability to enter cells via a form of active transport (endocytosis).

Data on magnetic hyperthermia on the 4T1 cells with Fe_3O_4:Y MNPs suggest that it can be used in future cancer treatment. This method can be better than chemotherapy, which has impact for viability of other healthy cells. The results showed that Fe_3O_4 NPs doped by 0.1% Y^{3+} ion reduced significantly the viability of cancer cells and can be better for future treatment applications than Fe_3O_4 without doping. The Fe_3O_4:0.1% Y NPs with a concentration of 35 μg/mL reduced the cell viability by 77% and with a concentration of 100 μg/mL, reduced the cell viability by 68% when the cells were exposed to the AMF for 30 min. In comparison, incubation with the MNPs without doping

reduced the cell viability by 85% when the cells were incubated with 35 μg/mL Fe_3O_4 NPs and approximately 72% with 100 μg/mL Fe_3O_4.

The Fe_3O_4 NPs additionally can be easily functionalized by antibodies for targeted drug therapy, which protects healthy cells from damages. In addition, the Fe_3O_4 NPs can be exploited for imaging and other diagnostic applications simultaneously, which is not possible by other hyperthermia processes.

■ ASSOCIATED CONTENT

Ⓢ Supporting Information

The Supporting Information is available free of charge at https://pubs.acs.org/doi/10.1021/acs.jpcc.9b11043.

> Calculation details and graphs of the lattice parameters of the all samples determined using the Rietveld method (PDF)

■ AUTHOR INFORMATION

Corresponding Author

Bozena Sikora — *Institute of Physics, Polish Academy of Sciences, PL-02668 Warsaw, Poland;* ⓞ orcid.org/0000-0001-5902-9682; Email: sikorab@ifpan.edu.pl

Authors

Przemyslaw Kowalik — *Institute of Physics, Polish Academy of Sciences, PL-02668 Warsaw, Poland*

Jakub Mikulski — *Institute of Physics, Polish Academy of Sciences, PL-02668 Warsaw, Poland*

Anna Borodziuk — *Institute of Physics, Polish Academy of Sciences, PL-02668 Warsaw, Poland*

Magdalena Duda — *Institute of Physics, Polish Academy of Sciences, PL-02668 Warsaw, Poland*

Izabela Kamińska — *Institute of Physics, Polish Academy of Sciences, PL-02668 Warsaw, Poland*

Karolina Zajdel — *Mossakowski Medical Research Centre, Polish Academy of Sciences, PL-02106 Warsaw, Poland*

Jaroslaw Rybusinski — *Institute of Experimental Physics, Faculty of Physics, University of Warsaw, PL-02093 Warsaw, Poland*

Jacek Szczytko — *Institute of Experimental Physics, Faculty of Physics, University of Warsaw, PL-02093 Warsaw, Poland*

Tomasz Wojciechowski — *Institute of Physics, Polish Academy of Sciences, PL-02668 Warsaw, Poland*

Kamil Sobczak — *Faculty of Chemistry, Biological and Chemical Research Centre, University of Warsaw, PL-02089 Warsaw, Poland*

Roman Minikayev — *Institute of Physics, Polish Academy of Sciences, PL-02668 Warsaw, Poland*

Magdalena Kulpa-Greszta — *Faculty of Chemistry, Rzeszow University of Technology, PL-35959 Rzeszow, Poland*

Robert Pazik — *Faculty of Biotechnology, University of Rzeszow, PL-35310 Rzeszow, Poland;* ⓞ orcid.org/0000-0002-4662-6688

Paulina Grzaczkowska — *Institute of Physics, Polish Academy of Sciences, PL-02668 Warsaw, Poland; Institute of Experimental Physics, Faculty of Physics, University of Warsaw, PL-02093 Warsaw, Poland*

Krzysztof Fronc — *Institute of Physics, Polish Academy of Sciences, PL-02668 Warsaw, Poland*

Mariusz Lapinski — *Department of Hypertension, Medical University of Warsaw, PL-02091 Warsaw, Poland*

Małgorzata Frontczak-Baniewicz — *Mossakowski Medical Research Centre, Polish Academy of Sciences, PL-02106 Warsaw, Poland*

Complete contact information is available at:
https://pubs.acs.org/10.1021/acs.jpcc.9b11043

Notes

The authors declare no competing financial interest.

■ REFERENCES

(1) Bate, G. *Magnetic Oxides Part 2*; Craik, D. J. John Wiley & Sons: New York, 1975, pp 705.

(2) Arruebo, M.; Fernández-pacheco, R.; Ibarra, M. R.; Santamaría, J. Magnetic nanoparticles for drug delivery. *Nano Today* **2007**, *2*, 22−32.

(3) Pradhan, P.; Giri, J.; Samanta, G.; Sarma, H. D.; Mishra, K. P.; Bellare, J.; Banerjee, R.; Bahadur, D. Comparative evaluation of heating ability and biocompatibility of different ferrite-based magnetic fluids for hyperthermia application. *J. Biomed. Mater. Res. B. Appl. Biomater.* **2007**, *81B*, 12−22.

(4) Huff, T. B.; Tong, L.; Zhao, Y.; Hansen, M. N.; Cheng, J. X.; Wei, A. Hyperthermic effects of gold nanorods on tumor cells. *Nanomedicine* **2007**, *2*, 125−132.

(5) Kim, D. H.; Nikles, D. E.; Brazel, C. S. Synthesis and characterization of multifunctional chitosan-$MnFe_2O_4$ nanoparticles for magnetic hyperthermia and drug delivery. *Materials* **2010**, *3*, 4051−4065.

(6) Kim, D. H.; Nikles, D. E.; Johnson, D. T.; Brazel, C. S. Heat generation of aqueously dispersed $CoFe_2O_4$ nanoparticles as heating agents for magnetically activated drug delivery and hyperthermia. *J. Magn. Magn. Mater.* **2008**, *320*, 2390−2396.

(7) Na, H. B.; Song, I. C.; Hyeon, T. Inorganic nanoparticles for MRI contrast agents. *Adv. Mater.* **2009**, *21*, 2133−2148.

(8) van Landeghem, F. K. H.; Maier-Hauff, K.; Jordan, A.; Hoffmann, K.-T.; Gneveckow, U.; Scholz, R.; Thiesen, B.; Brück, W.; von Deimling, A. Post-mortem studies in glioblastoma patients treated with thermotherapy using magnetic nanoparticles. *Biomaterials* **2009**, *30*, 52−57.

(9) Schulz, M. J.; Shanov, V. N.; Yun, Y. *Nanomedicine design of particles, sensors, motors, implants, robots, and devices*; Artech House: MA, USA 2009, p.549.

(10) Thapa, D.; Palkar, V. R.; Kurup, M. B.; Malik, S. K. Properties of magnetite nanoparticles synthesized through a novel chemical route. *Mater. Lett.* **2004**, *58*, 2692−2694.

(11) Lee, J. H.; Huh, Y. M.; Jun, Y.; Seo, J.; Jang, J.; Song, H. T.; Kim, S.; Cho, E. J.; Yoon, H. G.; Suh, J. S.; et al. Artificially engineered magnetic nanoparticles for ultra-sensitive molecular imaging. *Nat. Med.* **2007**, *13*, 95−99.

(12) Mendoza-Garcia, A.; Sun, S. Recent advances in the high-temperature chemical synthesis of magnetic nanoparticles. *Adv. Funct. Mater.* **2016**, *26*, 3809−3817.

(13) Wu, L.; Mendoza-Garcia, A.; Li, Q.; Sun, S. Organic phase syntheses of magnetic nanoparticles and their applications. *Chem. Rev.* **2016**, *116*, 10473−10512.

(14) Zhao, Z.; Chi, X.; Yang, L.; Yang, R.; Ren, B. W.; Zhu, X.; Zhang, P.; Gao, J. Cation exchange of anisotropic-shaped magnetite nano-

particles generates high-relaxivity contrast agents for liver tumor imaging. *Chem. Mater.* **2016**, *28*, 3497−3506.

(15) Szczerba, W.; Żukrowski, J.; Przybylski, M.; Sikora, M.; Safonova, O.; Shmeliov, A.; Nicolosi, V.; Schneider, M.; Granath, T.; Oppmann, M.; et al. Pushing up the magnetisation values for iron oxide nanoparticles via zinc doping: X-ray studies on the particle's sub-nano structure of different synthesis routes. *Phys. Chem. Chem. Phys.* **2016**, *18*, 25221−25229.

(16) Bram, S.; Gordon, M. N.; Carbonell, M. A.; Pink, M.; Stein, B. D.; Morgan, D. G.; Aguilà, D.; Aromi, G.; Skrabalak, S. E.; Losovyj, Y.; et al. Zn²⁺ ion surface enrichment in doped iron oxide nanoparticles leads to charge carrier density enhancement. *ACS Omega* **2018**, *3*, 16328−16337.

(17) Liang, X.; Wang, X.; Zhuang, J.; Chen, Y.; Wang, D.; Li, Y. Synthesis of nearly monodisperse iron oxide and oxyhydroxide nanocrystals. *Adv. Funct. Mater.* **2006**, *16*, 1805−1813.

(18) Colognato, R.; Bonelli, A.; Bonacchi, D.; Baldi, G.; Migliore, L. Analysis of cobalt ferrite nanoparticles induced genotoxicity on human peripheral lymphocytes: comparison of size and organic grafting-dependent effects. *Nanotoxicology* **2007**, *1*, 301−308.

(19) Pacchierotti, F.; Bellusci, M.; La Barbera, A.; Padella, F.; Mancuso, M.; Pasquo, A.; Grollino, M. G.; Leter, G.; Nardi, E.; Cremisini, C.; Giardullo, P. Biodistribution and acute toxicity of a nanofluid containing manganese iron oxide nanoparticles produced by a mechanochemical process. *Int. J. Nanomed.* **2014**, *9*, 1919−1929.

(20) Asmatulu, R.; Garikapati, A.; Misak, H. E.; Song, Z.; Yang, S.-Y.; Wooley, P. Cytotoxicity of magnetic nanocomposite spheres for possible drug delivery systems. *ASME Int. Mech. Eng. Congr. Expo.* **2012**, *10*, 911−918.

(21) Jang, J.-t.; Nah, H.; Lee, J.-H.; Moon, S. H.; Kim, M. G.; Cheon, J. Critical enhancements of MRI contrast and hyperthermic effects by dopant-controlled magnetic nanoparticles. *Angew. Chem., Int. Ed.* **2009**, *48*, 1234−1238.

(22) Zhu, S.; Xu, X.; Rong, R.; Li, B.; Wang, X. Evaluation of zinc-doped magnetite nanoparticle toxicity in the liver and kidney of mice after sub-chronic intragastric administration. *Toxicol. Res.* **2016**, *5*, 97−106.

(23) Groman, E. V.; Bouchard, J. C.; Reinhardt, C. P.; Vaccaro, D. E. Ultrasmall mixed ferrite colloids as multidimensional magnetic resonance imaging, cell labeling, and cell sorting agents. *Bioconjugate Chem.* **2007**, *18*, 1763−1771.

(24) De Silva, C. R.; Smith, S.; Shim, I.; Pyun, J.; Gutu, T.; Jiao, J.; Zheng, Z. Lanthanide(III)-doped magnetite nanoparticles. *J. Am. Chem. Soc.* **2009**, *131*, 6336−6337.

(25) Milanović, M.; Moshopoulou, E. G.; Stamopoulos, D.; Devlin, E.; Giannakopoulos, K. P.; Kontos, A. G.; Eleftheriadis, K.; Gini, M. I.; Nikolić, L. M. Structure and magnetic properties of $Zn_{1-x}In_xFe_2O_4$ and $ZnY_xFe_{2-x}O_4$ nanoparticles prepared by coprecipitation. *Ceram. Int.* **2013**, *39*, 3235−3242.

(26) Verma, S.; Chand, J.; Singh, M. Effect of In³⁺ ions doping on the structural and magnetic properties of $Mg_{0.2}Mn_{0.5}Ni_{0.3}In_xFe_{2-x}O_4$ spinel ferrites. *J. Magn. Magn. Mater.* **2012**, *324*, 3252−3260.

(27) Ishaque, M.; Islam, M. U.; Khan, M. A.; Rahman, I. Z.; Genson, A.; Hampshire, S. Structural, electrical and dielectric properties of yttrium substituted nickel ferrites. *Phys. Rev. B: Condens. Matter* **2010**, *405*, 1532−1540.

(28) Shinde, T. J.; Gadkari, A. B.; Vasambekar, P. N. Effect of Nd³⁺ substitution on structural and electrical properties of nanocrystalline zinc ferrite. *J. Magn. Magn. Mater.* **2010**, *322*, 2777−2781.

(29) Xing, Q.; Peng, Z.; Wang, C.; Fu, Z.; Fu, X. Doping effect of Y³⁺ ions on the microstructural and electromagnetic properties of Mn−Zn ferrites. *Phys. B* **2012**, *407*, 388−392.

(30) Shirsath, S. E.; Toksha, B. G.; Jadhav, K. M. Structural and magnetic properties of In³⁺ substituted $NiFe_2O_4$. *Mater. Chem. Phys.* **2009**, *117*, 163−168.

(31) Cvejić, Z.; Rakić, S.; Jankov, S.; Skuban, S.; Kapor, A. Dielectric properties and conductivity of zinc ferrite and zinc ferrite doped with yttrium. *J. Alloys Compd.* **2009**, *480*, 241−245.

(32) Hashim, M.; Alimuddin; Kumar, S.; Shirsath, S. E.; Kotnala, R. K.; Chung, H.; Kumar, R. Structural properties and magnetic interactions in $Ni_{0.5}Mg_{0.5}Fe_{2-x}Cr_xO_4$ (0≤x≤1) ferrite nanoparticles. *Powder Technol.* **2012**, *229*, 37−44.

(33) Yonezawa, M.; Otsuka, T.; Matsui, N.; Tsuji, H.; Kato, K. H.; Moriyama, A.; Kato, T. Hyperthermia induces apoptosis in malignant fibrous histiocytoma cells in vitro. *Int. J. Cancer* **1996**, *66*, 347−351.

(34) Sellins, K. S.; Cohen, J. J. hyperthermia induces apoptosis in thymocytes. *Radiat. Res.* **1991**, *126*, 88−95.

(35) Christophi, C.; Winkworth, A.; Muralihdaran, V.; Evans, P. The treatment of malignancy by hyperthermia. *Surg. Oncol.* **1998**, *7*, 83.

(36) Welch, A. J.; Motamedi, M.; Rastegar, S.; LeCarpentier, G. L.; Jansen, D. Laser thermal ablation. *Photochem. Photobiol.* **1991**, *53*, 815−823.

(37) Goldstein, L. S.; Dewhirst, M. W.; Repacholi, M.; Kheifets, L. Summary, conclusions and recommendations: adverse temperature levels in the human body. *Int. J. Hyperthermia* **2009**, *19*, 373−384.

(38) Jaque, D.; Maestro, L. M.; del Rosal, B.; Haro-Gonzalez, P.; Benayas, A.; Plaza, J. L.; Rodríguez, E. M.; Solé, J. G. Nanoparticles for photothermal therapies. *Nanoscale* **2014**, *6*, 9494−9530.

(39) Raaphorst, G. P.; Freeman, M. L.; Dewey, W. C. Radiosensitivity and recovery from radiation damage in cultured CHO cells exposed to hyperthermia at 42.5 or 45.5 degrees C. *Radiat. Res.* **1979**, *79*, 390−402.

(40) Dutz, S.; Hergt, R. Magnetic particle hyperthermia — a promising tumour therapy? *Nanotechnology* **2014**, *25*, 452001.

(41) Zhang, Y.; Zhai, Y. Magnetic induction heating of nano-sized ferrite particle. In *advances in induction and microwave heating of mineral and organic materials*; Stanislaw Grundas, IntechOpen, 2011, 483−502.

(42) Dunlop, D. J. Superparamagnetic and single-domain threshold sizes in magnetite. *J. Geophys. Res.* **1973**, *78*, 1780−1793.

(43) Carrey, J.; Mehdaoui, B.; Respaud, M. Simple models for dynamic hysteresis loop calculations of magnetic single-domain nanoparticles: Application to magnetic hyperthermia optimization. *J. Appl. Phys.* **2011**, *109*, No. 083921.

(44) Dutz, S.; Hergt, R. Magnetic nanoparticle heating and heat transfer on a microscale: Basic principles, realities and physical limitations of hyperthermia for tumour therapy. *Int. J. Hyperthermia* **2013**, *29*, 790−800.

(45) Jordan, A.; Scholz, R.; Wust, P.; Schirra, H.; Schiestel, T.; Schmidt, H.; Felix, R. Endocytosis of dextran and silan-coated magnetite nanoparticles and the effect of intracellular hyperthermia on human mammary carcinoma cells in vitro. *J. Magn. Magn. Mater.* **1999**, *194*, 185−196.

(46) Jordan, A.; Scholz, R.; Wust, P.; Fähling, H.; Felix, R. Magnetic fluid hyperthermia (MFH): Cancer treatment with AC magnetic field induced excitation of biocompatible superparamagnetic nanoparticles. *J. Magn. Magn. Mater.* **1999**, *201*, 413−419.

(47) Nasongkla, N.; Bey, E.; Ren, J.; Ai, H.; Khemtong, C.; Guthi, J. S.; Chin, S. F.; Sherry, A. D.; Boothman, D. A.; Gao, J. Multifunctional polymeric micelles as cancer-targeted, MRI-ultrasensitive drug delivery systems. *Nano Lett.* **2006**, *6*, 2427−2430.

(48) Mornet, S.; Vasseur, S.; Grasset, F.; Duguet, E. Magnetic nanoparticle design for medical diagnosis and therapy. *J. Mater. Chem.* **2004**, *14*, 2161−2175.

(49) Kowalik, P.; Elbaum, D.; Mikulski, J.; Fronc, K.; Kaminska, I.; Morais, P. C.; De Souza, P. E.; Nunes, R. B.; Veiga-Souza, F. H.; Gruzel, G.; et al. Upconversion fluorescence imaging of HeLa cells using ROS generating SiO_2-coated lanthanide-doped $NaYF_4$ nanoconstructs. *RSC Adv.* **2017**, *7*, 30262−30273.

(50) Hong, J. H.; Kim, W. S.; Lee, J. I.; Hur, N. H. Exchange coupled magnetic nanocomposites of $Sm(Co_{1-x}Fe_x)_5$ / Fe_3O_4 with core/shell structure. *Solid State Commun.* **2007**, *141*, 541−544.

(51) Klug, P.; Alexander, L. E. *X-ray diffraction procedure*; Wiley: New York, 1954.

(52) Shannon, R. D. Revised effective ionic radii and systematic studies of interatomic distances in halides and chalcogenides. *Acta Cryst.* **1976**, *32*, 751−767.

(53) Neel, L. Magnetic properties of ferrites: ferrimagnetism and antiferromagnetism. *Ann. Phys.* **1948**, *3*, 137−198.

(54) Ortega, D.; Pankhurst, Q. A. *Nanoscience: Volume 1: Nanostructures through Chemistry*; O'Brien, P., Royal Society of Chemistry, 2012, 60−88.

(55) Kallumadil, M.; Tada, M.; Nakagawa, T.; Abe, M.; Southern, P.; Pankhurst, Q. A. Suitability of commercial colloids for magnetic hyperthermia. *J. Magn. Magn. Mater.* **2009**, *321*, 1509−1513.

(56) Bonvin, D.; Arakcheeva, A.; Millán, A.; Piñol, R.; Hofmann, H.; Ebersold, M. M. Controlling structural and magnetic properties of IONPs by aqueous synthesis for improved hyperthermia. *RSC Adv.* **2017**, *7*, 13159.

(57) Surowiec, A.; Miaskowski, Z.; Budzyński, M. Investigation of magnetite Fe_3O_4 nanoparticles for magnetic hyperthermia. *Nukleonika* **2017**, *62*, 183−186.

(58) Bordelon, D. E.; Cornejo, C.; Grüttner, C.; Westphal, F.; DeWeese, T. L.; Ivkov, R. Magnetic nanoparticle heating efficiency reveals magneto-structural differences when characterized with wide ranging and high amplitude alternating magnetic fields. *J. Appl. Phys.* **2011**, *109*, 124904.

(59) Kolenko, Y. V.; Bañobre-López, M.; Rodróguez-Abreu, C.; Carbó-Argibay, E.; Sailsman, A.; Piñeiro-Redondo, Y.; Cerqueira, M. F.; Petrovykh, D. Y.; Kovnir, K.; Lebedev, O. I.; et al. Large-scale synthesis of colloidal Fe_3O_4 nanoparticles exhibiting high heating efficiency in magnetic hyperthermia. *J. Phys. Chem. C* **2014**, *118*, 8691−8701.

(60) Lima, E., Jr.; De Biasi, E.; Vasquez Mansilla, M.; Saleta, M. E.; Granada, M.; Troiani, H. E.; Effenberger, F. B.; Rossi, L. M.; Rechenberg, H. R.; Zysler, R. D. Heat generation in agglomerated ferrite nanoparticles in an alternating magnetic field. *J. Phys. D: Appl. Phys.* **2013**, *46*, No. 045002.

(61) Prasad, N. K.; Rathinasamy, K.; Panda, D.; Bahadur, D. Mechanism of cell death induced by magnetic hyperthermia with nanoparticles of γ-$Mn_xFe_{2-x}O_3$ synthesized by a single step process. *J. Mater. Chem.* **2007**, *17*, 5042−5051.

(62) Thorat, N. D.; Otari, S. V.; Patil, R. M.; Khot, V. M.; Prasad, A. I.; Ningthoujam, R. S.; Pawar, S. H. Enhanced colloidal stability of polymer coated $La_{0.7}Sr_{0.3}MnO_3$ nanoparticles in physiological media for hyperthermia application. *Colloids Surf., B* **2013**, *111*, 264−269.

(63) Patil, R. M.; Thorat, N. D.; Shete, P. B.; Otari, S. V.; Tiwale, B. M.; Pawar, S. H. In vitro hyperthermia with improved colloidal stability and enhanced SAR of magnetic core/shell nanostructures. *Mater. Sci. Eng., C* **2016**, *59*, 702−709.